fluids

MDPI

Article

Simulation of Particle Structure Rearrangement and Reaction in Wall-Flow Filters at High Flow Velocities with Lattice Boltzmann Methods

Christoph Gaul [1,2], Ole Desens [2,3,*], Pascal Ernst [1], Andreas Nettekoven [1,2], Achim Dittler [2,3] and Mathias J. Krause [1,2,4]

[1] Lattice Boltzmann Research Group, Karlsruhe Institute of Technology, 76131 Karlsruhe, Germany; andreas.nettekoven@kit.edu (A.N.); mathias.krause@kit.edu (M.J.K.)
[2] Institute of Mechanical Process Engineering and Mechanics, Karlsruhe Institute of Technology, 76131 Karlsruhe, Germany; achim.dittler@kit.edu
[3] Gas Particle Systems, Karlsruhe Institute of Technology, 76131 Karlsruhe, Germany
[4] Institute for Applied and Numerical Mathematics, Karlsruhe Institute of Technology, 76131 Karlsruhe, Germany
* Correspondence: ole.desens@kit.edu

Abstract

Wall-flow filters are used in exhaust gas after treatment systems to reduce particulate matter emissions from internal combustion engines. The particles accumulate on the filter surface during operation, forming a layer that progressively increases the flow resistance and thus the pressure drop. This layer consists mostly of combustible materials but also contains inert ash parts. The pressure drop increase leads to the necessity of regenerating the filter. Filter regeneration may cause particle structure fragments to rearrange within single-filter channels, leading to specific ash deposition patterns that modify the filter's pressure drop, loading behavior, and separation efficiency. This work advances previous investigations toward application-relevant temperature and inflow-velocity conditions by extending the existing resolved-particle methodology with turbulence and reaction models, enabling temperature-dependent effects on particle-structure fragments to be considered. The rearrangement process is studied in detail. It can be shown that at high velocity, most gas crosses into the outlet channel at the end of the inflow channel, leading to a pressure spike. A fragment-local reaction model was introduced and shows qualitative agreement with the experimental results. These simulations also showed a temperature difference of about 15 K between particles at the beginning and end of the inlet channel, leading to faster oxidation close to the inlet. The presented modeling approach helps to assess the formation of deposition patterns and their influence on filter behavior, engine efficiency, fuel consumption, and long-term filter durability.

Keywords: wall-flow filter; regeneration; lattice Boltzmann methods; resolved particle simulations; homogenized lattice Boltzmann method

Academic Editor: Kannan Premnath

Received: 18 May 2026
Revised: 23 July 2026
Accepted: 30 July 2026
Published: 5 August 2026

1. Introduction

The global need to reduce air pollution and greenhouse-gas-related environmental impacts has led to increasingly strict emission regulations, making exhaust-gas aftertreatment systems essential for the operation of combustion engines [1]. Wall-flow filters, including diesel particulate filters, operate based on a pattern of alternating sealed inlet and outlet channels that force the exhaust stream through the porous walls, which filter out the

particles. Modern wall-flow filters achieve reliable separation efficiencies of >95–99% for both particle number and particle mass [2–5]. As the filter becomes increasingly loaded, particulate layers accumulate on the surfaces of the porous walls, leading to a rise in the filter pressure drop and a corresponding deterioration of engine performance [6–8]. The deposited particulate matter (PM) consists predominantly of combustible soot with minor fractions of inorganic, non-combustible ash, enabling filter regeneration through continuous or periodic oxidation of its reactive constituents. These resulting inhomogeneities can cause the originally continuous layer to fragment into discrete segments ("soot islands"), which may detach from the filter surface and relocate within the channel [6]. Consequently, characteristic ash deposition patterns influence the pressure drop contribution of an individual channel, its loading capacity, and its separation efficiency. In situ observations in a model filter channel confirmed that, during discontinuous regeneration with air at high gas velocities and sufficiently high temperatures, filter regeneration can trigger particle layer fragmentation as well as detachment and transport of individual fragments [9,10]. A number of studies [7,11–13] have addressed the question of which mechanisms drive the formation of these patterns, yet a consistent and broadly accepted explanation has not yet emerged. However, these transport processes are highly transient and occur on small spatial scales inside optically and geometrically constrained filter channels. Experiments provide essential phenomenological insight, but a direct quantification of local forces, fragment trajectories, particle–wall interactions, and temperature-dependent reaction rates remains challenging. Closing this gap is essential, since the resulting patterns directly affect engine efficiency, fuel economy and the operational lifetime of the filter. Numerical simulations can complement these measurements by resolving quantities that are difficult to access experimentally. In this context, the lattice Boltzmann method (LBM) is particularly attractive because it is well suited for complex geometries, porous media, and particle-laden flows.

In a sequence of prior publications, Hafen et al. [14–17] have progressively addressed selected facets of this problem. Hafen et al. [14] introduced an LBM-based framework for wall-flow filter simulations and demonstrated its ability to describe gas flow and particle fragment transport. The validation showed that the solution converged at a super-linear rate with increasing grid resolution and matched the established reference solution [18] closely. Building on this foundation, the second work [15] employed the framework to examine the detachment, acceleration and deceleration of individual PM layer fragments during filter regeneration. The third work [16] extended the model to simulate inlet velocities as high as $60\,\mathrm{m\,s^{-1}}$. Hafen et al. evaluated the stability and accuracy for both particle-free and particle-including flow configurations. When particle-layer fragments were included, the accessible parameter range was restricted to inlet velocities of $28\,\mathrm{m\,s^{-1}}$. In the most recent one [17], the model was extended by a discrete contact model for particle–particle and particle–wall collisions. This was then used to investigate the plug formation process in detail for inlet velocities between $4\,\mathrm{m\,s^{-1}}$ and $14\,\mathrm{m\,s^{-1}}$. Afterwards, a detailed parameter study was carried out, showing that the layer structure and the inflow velocity have the largest influence on the overall pressure drop.

The present work represents a sequel to previous work [17] by including both high-flow conditions of $60\,\mathrm{m\,s^{-1}}$, when particle-layer fragments are included, and the influence of temperature and reaction. The goal of this work is therefore the extension of the resolved particle methodology [14–17,19–21] with a turbulence model to stabilize particle simulations at higher Reynolds numbers. This is then used to study the break-up, detachment and transport of the fragments along the channel, as well as the plug formation process under a high inflow speed of $60\,\mathrm{m\,s^{-1}}$. This plug forms through the accumulation of PM fragments into an unordered porous packing that may take up a considerable part of the

channel volume [11,13,22,23]. To reproduce this behavior numerically, the model accounts for contacts among moving fragments, interactions between moving fragments and stationary fragments, and collisions with the channel walls. The second goal is the extension of the model to account for the influence of temperature and reaction of particle fragments, which is then compared with experimental data. In order to incorporate thermal effects on PM fragments, the simulation framework is extended by a dedicated temperature lattice. In each discrete reaction step, a volume-averaged temperature is computed for each PM fragment. This temperature is then used to determine the local oxidation rate and calculate the decreasing fragment volume.

2. Mathematical Modeling and Numerical Methods

Following Hafen et al. [16], the gas flow is governed by the incompressible Navier–Stokes equations (NSE) [24]. These equations are treated using the LBM, which yields the local velocity $\boldsymbol{u}(\boldsymbol{x}, t)$ and pressure $p(\boldsymbol{x}, t)$ at each position $\boldsymbol{x}$ and time t in the three-dimensional domain. Since the underlying numerical model has already been described in detail by Hafen et al. [16], the corresponding equations are not repeated in the present manuscript. It covers the LBM fundamentals, the modeling of porous media and resolved particle surfaces, and the quantification of discretization errors and convergence properties. The extension toward discrete particle contacts is adopted from Hafen et al. [17]. This work therefore only contains the explanation of the turbulence model, heat transfer, advection–diffusion simulation with LBM and the Arrhenius model used for reaction speed.

2.1. Thermal and Reaction Model

To calculate the local reaction speed of individual soot fragments, the average temperature of each fragment has to be determined. Therefore, the simulation setup is expanded by a second lattice, solving the heat transfer equation in the form of an advection–diffusion equation (ADE):

$$\frac{\partial T}{\partial t} + \boldsymbol{u} \cdot \nabla T = \kappa \nabla^2 T + Q \tag{1}$$

with temperature T, velocity $\boldsymbol{u}$ and given thermal diffusivity κ as well as heat source Q.

Similarly to the Navier–Stokes equation, the advection–diffusion equation can also be modeled with the LBM [25]. Changing the equilibrium function used is sufficient. The general LB algorithm is therefore unchanged:

$$g_i(x + c_i \Delta t, t + \Delta t) - g_i(x, t) = \Omega_i(x, t) + Q_i(x, t) \tag{2}$$

In this equation, g_i is the discrete-velocity distribution function, Ω_i is the collision operator and Q_i is used to account for sources.

Here, the simple Bhatnagar–Gross–Krook (BGK) operator was used for the collision:

$$\Omega_i(x, t) = -\frac{\Delta t}{\tau_g}(g_i(x, t) - g_i^{eq}(x, t)) \tag{3}$$

with the relaxation time of the fluid τ_g,

$$\tau_g = \frac{\kappa}{c_s^2} + \frac{1}{2}\Delta t \tag{4}$$

and the equilibrium distribution function

$$g_i^{eq}(T, u) = w_i T \left(1 + \frac{c_i \cdot u}{c_s^2}\right) \tag{5}$$

$c_s = \frac{1}{\sqrt{3}}$ is the lattice speed of sound, c_i are the discrete velocities and w_i are the weights.

The macroscopic temperature can be obtained from

$$T(x,t) = \sum_i g_i(x,t). \tag{6}$$

Because only the zeroth moment is relevant, a reduced stencil of D3Q7 or D2Q5 can be used when discretizing the ADE with the LBM.

The above method can be used to simulate heat flow in a single phase. To model the heat transfer in porous particles, it has to be modified to account for the different conductivity of the particles and the transition phase.

To set the local heat conductivity, the local relaxation time τ_g has to be modified, as described in Equation (4). The local heat conductivity is set by tracking the position and angles of the respective particles and setting the local relaxation time for each cell.

The reaction rates of the particles are temperature-dependent and are described through the Arrhenius equation:

$$\frac{\partial \alpha}{\partial t} = -k_{0,ox} \cdot \beta \cdot \exp\left[\frac{-E_a}{R \cdot T}\right] \cdot \alpha^n \tag{7}$$

This approach is based on the global kinetic approach described by Hagen et al. [26] and used by Desens et al. [10] on the experimental wall-flow filter. The average temperature of each particle is used to calculate the local reaction temperature, with $\alpha = \frac{m}{m_0}$, $\beta = \frac{\partial T}{\partial t} = 5.0\,\mathrm{K\,min^{-1}}$, the constant heating rate used in the temperature-programmed oxidation (TPO) experiment, $k_{0,ox}$ the pre-exponential factor of the rate coefficient, E_a being the activation energy and n the reaction order. Oxygen is supplied in excess during the TPO experiment and regeneration simulation, so p_{O_2} is assumed to remain constant. This constant contribution is absorbed into the effective pre-exponential factor $k_{0,ox}$, which allows the oxygen-order term to be omitted from the explicit rate expression in Equation (7). For this work, the pre-exponential factor, reaction order and activation energy derived from Desens et al. [10] for carbon black are used. These are $k_{0,ox} = 3.59 \times 10^6\,\mathrm{s^{-1}}$, $n = 0.95$ and $E_a = 162\,\mathrm{kJ\,mol^{-1}}$. The Arrhenius parameters are material-specific, since soot reactivity depends strongly on fuel type, formation conditions, nanostructure, and chemical composition [26–28]. Changing the activation energy, pre-exponential factor, or reaction order would directly affect the predicted oxidation rate.

The mass difference in a reaction interval is calculated from $\Delta m = \frac{\partial \alpha}{\partial t} \cdot m_0 \Delta t$, which can be used to calculate both the volume decrease and the increase in temperature via the reaction enthalpy of pure carbon.

2.2. Turbulence Modeling

In previous works [14–17,19] reduced velocities had to be used for the simulation, because fully resolving the turbulence in the wall-flow filter was not possible.

To offset this, the large eddy Smagorinsky model is used to model the turbulence in the simulation. This model imposes an artificial viscosity ν_{turb}, which is calculated from the Smagorinsky constant C_S and the shear stress tensor $S_{\alpha,\beta}$.

$$\nu_{turb} = (C_S)^2 \cdot \sqrt{2 \sum_{\alpha,\beta} S_{\alpha\beta} S_{\alpha\beta}} \tag{8}$$

This turbulent viscosity is then added to the laminar viscosity ν_0 to form the effective viscosity $\nu_{eff} = \nu_{turb} + \nu_0$.

The strain rate can be locally calculated from the non-equilibrium populations [25].

$$S_{\alpha,\beta} = -\frac{1}{2\rho\tau^* c_s^2} \sum_q e_{i,\alpha} e_{i,\beta} (f_i - f_i^{eq}) \tag{9}$$

with $\tau^* = \frac{\nu_{eff}}{c_s^2} + \frac{1}{2}$, which is the modified relaxation time, calculated from the effective viscosity. The Smagorinsky constant is chosen as $C_S = 0.14$, as is common in engineering applications; this is backed up by literature values from Pope [29], as well as earlier numerical studies [30,31]. The lattice speed of sound is given as $c_s = \frac{1}{\sqrt{3}}$.

The thermal diffusivity is also modified analogously to account for turbulent mixing:

$$\kappa_{eff} = \kappa_0 + \frac{\nu_{turb}}{Pr_t} \tag{10}$$

The turbulent Prandtl number Pr_t correlates the turbulent momentum transport to the turbulent heat transfer. In simple turbulent flows it is of the order of one (see Pope [29]) and has been chosen in this work as $Pr_t = 0.86$, based on common applications.

To prevent calculations of contacts between static particles in the end plug in the channel, the kinetic energy of particles is used as a threshold to deactivate the movement of stationary particles. Analogous to Hafen et al. [17], it is calculated from the particle's moment of inertia I_p, its mass m_p, its velocity u_p and its rotational velocity ω_p, which represent its translational and rotational energy $\mathrm{Y}_{p,trans}$ and $\mathrm{Y}_{p,rot}$.

$$\mathrm{Y}_{p,\mathrm{kin}} = \mathrm{Y}_{p,\mathrm{trans}} + \mathrm{Y}_{p,\mathrm{rot}} = \frac{m_p u_p^2}{2} + \frac{I_p \boldsymbol{\omega}_p^2}{2} \tag{11}$$

When a particle's kinetic energy is under a threshold due to being stationary in a cluster of other non-moving particles, its movement is no longer considered. This reduces the computational load significantly, because in a plug every particle touches several other particles at the same time and these collisions would have to be calculated in every timestep. In addition, the cumulative kinetic energy

$$\mathrm{Y}_{\mathrm{kin}} = \sum_{p=0}^{N_p} \mathrm{Y}_{p,\mathrm{kin}} \tag{12}$$

can be used to quantify the overall state of the rearrangement process.

3. Application to a Wall-Flow Filter

This work uses the same simulation setup as previous works [14–16,19] of a hash-shaped wall-flow filter, with an overall length of $l_x = 24\,\mathrm{mm}$. The porous walls of the filter have a thickness of $l_w = 0.4\,\mathrm{mm}$. The central square channel has a width and height of four times the wall thickness at $l_y = 1.6\,\mathrm{mm}$. It is surrounded by half- and quarter-sized channels. The quarter-sized channels are square with a side length of 0.2 mm, while the half-sized channels are rectangular with a size of $0.2 \times 0.4\,\mathrm{mm}$. The four quarter-sized and the center channel act as inflow channels, while the half-sized channels act as outflow channels. The channel ends are blocked by walls accordingly; see Figure 1. This forces the fluid to flow through the porous walls of the filter.

Pressure-related quantities are used for relative comparisons within this work. The model's ability to predict absolute pressure drops for full-length channels has already been verified against literature data [14] and experimental measurements [15]. In this study, the influence of temperature is taken into account. Instead of assuming ambient air as in the previous works, in this case air at 873 K and ambient pressure are used.

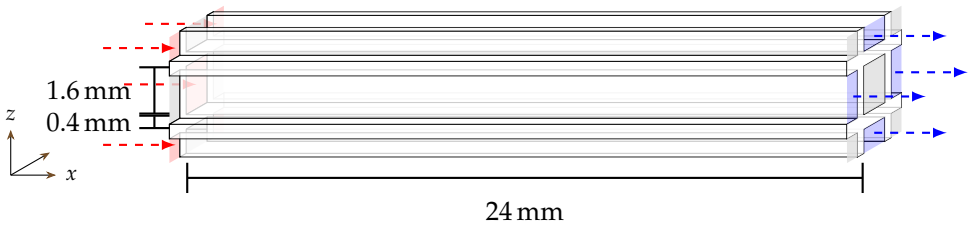

Figure 1. Schematic sketch of the wall-flow filter model, consisting of one central inflow (red) channel with fractions of surrounding inflow and outflow (blue) channels separated by porous walls [17].

Dirichlet velocity and pressure conditions are used on inlet and outlet, respectively, prescribing a flow with constant mass flow rates at the inlet. These are realized through the LBM-specific regularized local boundary conditions [32] at the inlets and interpolated boundary conditions [33] at the outlets. To suppress numerical instabilities caused by steep velocity and pressure gradients at the start of the transient simulation, the inflow velocity is slowly ramped up. The end cap walls of the channels prescribe a no-slip boundary. This is achieved through the LBM-specific bounce-back boundary condition [34]. The open sides are periodic, mimicking a real wall-flow filter with hundreds of these channels. The discretization N describes the number of cells per channel width l_w. For the temperature lattice, Dirichlet boundary conditions, prescribing a constant temperature, are used for the inlet, periodic (on the surrounding sides) and zero-gradient Neumann boundary conditions on outlets and walls.

For the second part, the computational domain is reduced to the two-channel model described in [35] to resemble the experimental setup.

As the present work extends the setup of its predecessor [16], it also uses the same setup for modeling a deposition layer of soot on the walls of the filter, which slowly breaks up during the simulations. The initial setup of individual fragments of this decomposing layer are described through a regular 3×50 array of identical cubic discs that cover the porous walls of the center channel. During the velocity ramp-up phase at the beginning of the simulation, these particles are held in place artificially. The simulation is then run until convergence, which is defined by a residuum average energy. After this, the fragments are released.

The decomposition of the deposition layer is random in the real process. To ensure reproducibility of the simulation results, this is not considered in the setup. As the channel is symmetric, multiple uniform fragments detach simultaneously, leading to an accelerated rearrangement process than would occur in an experimental or real filter channel. The simulation is then run until the cumulative kinetic energy (see Equation (12)) of the fragments falls below a predefined energy threshold.

Material parameters for the fluid representing air have been taken from [36] and for the soot particles from [14,26]. The chosen parameters are listed in Table 1.

Table 1. Overview of material parameters.

Material	ρ/kg m^{-3}	ν/m^2 s^{-1}	c_p/kJ kg^{-1} K^{-1}	λ/mW m^{-1} K^{-1}
Air	0.31	1505.7×10^{-7}	1.163	73.82
Particles	500	-	0.9	120

The first part of this paper focuses on the detachment and deposition at realistic channel length and inflow velocity. Here, the same parameters as in [17] are used with realistic velocity and channel length, using the previously described LES model for stabilization.

The second part focuses on reaction. In these simulations, fragment-local reaction and a temperature field are included. These simulations are then compared to recent

experiments in a model filter channel [9,10,37]. In these experiments, soot generated by fuel-rich propane combustion is used. It does not contain inert parts. A time scale of >20 min in the experiment for the reaction is not realistic for simulation. Therefore, instead of running the entire simulation, several simulations at different states of the regeneration are run to check if the trajectory of the pressure loss is correct.

The simulation is divided into two consecutive parts:

- Fluid velocity ramp-up.
- Reaction.

Previous papers [14,17,19] focused on the ramp-up phase and convergence of laminar flow, the second one on the detachment and the third one on the forming of plugs from ash fragments and a parameter study. The first part of this paper will focus on plug formation at realistic flow speed, and the second part will focus on the reaction of stationary particles. Parameters for the discrete contact model are kept constant from the last work by Hafen et al. [17].

4. Results and Discussion

In the first part, the influence of a realistic inlet velocity of $\bar{u}_{in} = 60\,\mathrm{m\,s^{-1}}$ on the rearrangement process and plug formation is studied. Because of stability issues in previous works [14], a LES model is introduced, as described in Section 2.2. This allows for a reduced resolution compared to [17] to be used ($N = 60$) while increasing the inflow velocity from $\bar{u}_{in} = 10\,\mathrm{m\,s^{-1}}$ to $60\,\mathrm{m\,s^{-1}}$. The second part addresses the reaction of the deposited fragments under the conditions of the model filter channel experiment. An overview of all cases considered in this work is given in Table 2.

Table 2. Overview of experimental and numerical cases considered.

Case	Geometry and Length	N	$\bar{u}_{in}$/m s^{-1}	T/K	Fragment Count
Rearrangement simulation	wall-flow filter channel model [17], 24 mm	60	60	873	3×50 fragments per wall
Reaction simulation	reduced two-channel model [14], 120 mm	60	60	823	600 fragments
Regeneration experiment	model filter channel [9], 120 mm	–	60	823	soot layer (≈690 at 8 min)

4.1. Rearrangement at High Flow Velocities

The setup is oriented on the fragmented deposition layer base configuration reported by Hafen et al. [17]. It uses fragments with a height of 170 µm, an equilateral width of 340 µm, and 50 fragment rows along the channel. A particle density of $500\,\mathrm{kg\,m^{-3}}$ and a fragment modulus of elasticity of 0.1 MPa are prescribed. The analysis distinguishes between the converged fragmented-layer state, the transient rearrangement behavior (cf. Section 4.1.1), and the resulting plug state (cf. Section 4.1.2).

4.1.1. Flow Field and Transient Behavior

The resulting flow field is visualized through streamlines in Figure 2; the contour color of the streamlines shows the local velocity magnitude $|u|$. It is clearly visible that the flow is up to 5 times faster in the inflow channels, with velocities reaching from 60 to 100 m s^{-1}, than in the outflow channels. The velocity decreases along the length of the inflow channel and increases in the outlet channels in correspondence. Along the length of the outlet channel, a regular Poiseuille profile starts to form.

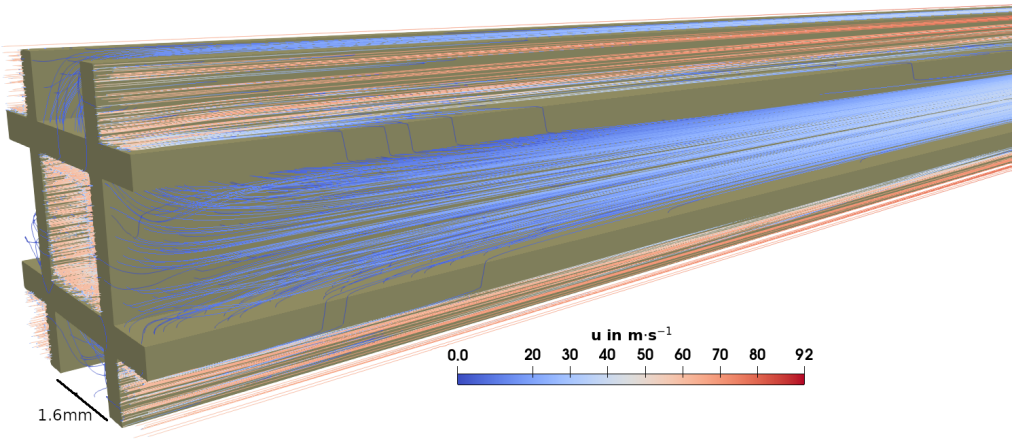

Figure 2. Flow field with streamlines exhibiting local flow direction. Color scale indicates local velocity magnitude.

As the fragments detach from the wall, the configuration slowly transitions from a uniformly fragmented deposition layer to an immobile plug configuration. This transition is shown in Figure 3 at five uniform steps in time from $t_1 = 2.5\,\text{ms}$ to $t_5 = 12.5\,\text{ms}$; shown is the inner view of the central channel. Analogous to Hafen et al. [17], the cumulative kinetic energy serves as a termination criterion for the rearrangement process. It increases during fragment detachment and transport, but it decreases again as the fragments settle into the plug state and approaches nearly zero at t_5. At t_1 the uniformly fragmented PM layer is visible. Due to the effectively decreased cross-sectional area of the channel, the local velocity increases up to $\approx 100\,\text{m}\,\text{s}^{-1}$ in the entire channel compared to the inlet boundary condition of $60\,\text{m}\,\text{s}^{-1}$. The pressure drop between inlet and outlet quickly settles to a constant $\Delta p = 27\,\text{hPa}$.

As the fragments start to detach from the wall, beginning at t_2 the local velocity returns from its elevated state back to the velocity of the inflow boundary condition in regions no longer covered by fragments. To the right of the detached fragments a dead-zone with reduced velocity starts to form. This forces more fluid through the porous walls, thus resulting in an increase in pressure drop. Afterwards, the fragments are quickly pushed back through the channel, until an agglomeration is formed at t_3, effectively blocking flow behind it. This causes a pressure spike at the front end of the agglomeration and a drastic pressure and velocity decrease in the dead-zone behind it. At the same time, a minor plug is starting to build up at the very end of the channel. During this time, left of the agglomeration, the cross-section starts to clear up and the pressure drop starts to fall again. The agglomeration is then slowly pushed back through the channel in t_4, while at the same time the back plug is slowly increasing in size. At t_5, the agglomeration reaches the plug at the end of the channel. At this point, the fragments become mostly stationary. This plug consists of a dense multi-row arrangement of fragments. Most particulate matter is now concentrated within the plug at the very end of the channel, with some sticking to the walls directly in front of the plug. In this final state the pressure drop once again reaches a constant value of $\Delta p = 19\,\text{hPa}$. This results from an increased cross-section and a longer open flow area through the porous walls, which is in turn balanced by the reduced overall length of the channel caused by the plug.

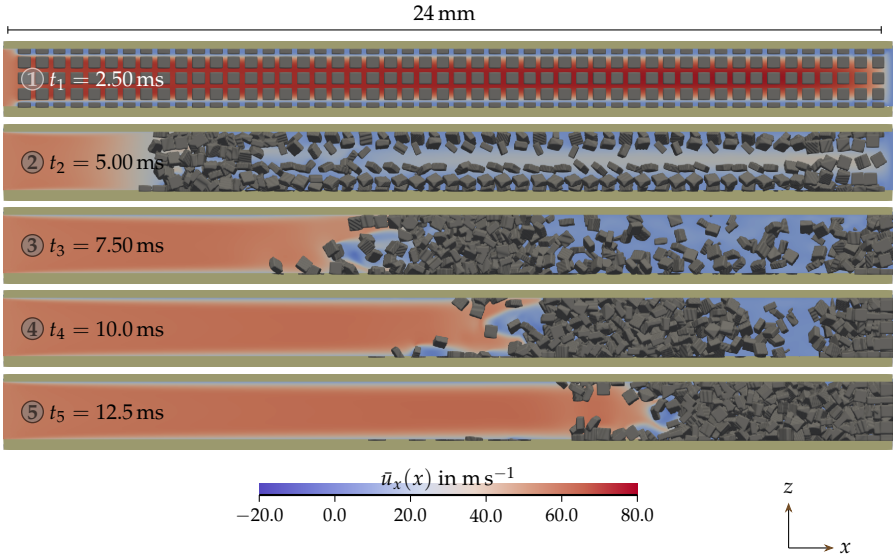

Figure 3. Time series of detachment, transport and plug formation. Dark yellow structures represent porous filter substrate and fragmented PM layer in gray.

4.1.2. Plug State

The transient behavior ends with the formation of the plug state in which transported fragments have accumulated into a stable plug-like packing at the end of the channel. Figure 4 shows the plug state density in comparison to the mean density in the fragmented state. It can be seen that in the plug state, the density is zero up to $x = 10\,\text{mm}$, then shows a small increase and then increases rapidly at $x = 16\,\text{mm}$, until it reaches a near constant value of $\rho = 294\,\text{kg m}^{-3}$ in the last third of the channel length. This value is only slightly larger than the one calculated by Hafen et al. [17]. A direct comparison with the literature requires care since the simulated fragments consist of soot with a prescribed particle density of $\rho_p = 500\,\text{kg m}^{-3}$, whereas the channel-end plugs characterized by Kimura et al. [22], Sappok et al. [23], and Dittler [11] are formed from lube-oil-derived ash as a residual from periodic filter regeneration and soot removal. Reported packing densities of ash end plugs lie between 100 and 400 kg m^{-3} [22,23,38], with Kimura et al. [22] reporting 235 kg m^{-3}. Such ash plugs develop only after a large number of regeneration cycles, during which the ash itself may sinter, compact or otherwise change its morphology, whereas the soot agglomerates simulated here represent the transport mechanism by which the ash is carried towards the channel end in the first place.

Figure 5 compares the axial velocity profile $\bar{u}_x(x)$ and the pressure profile $\bar{p}(x)$ in the central inflow channel and in the outflow channel for the fragmented-layer and plug states. Mean velocities in both inflow and outflow channels are shown; this shows a continuous decrease in velocity along the length of the inflow channel and a corresponding increase in velocity in the outlet channels. The velocity and pressure profiles are measured as averages over the inlet and outlet channel width. This ensures that higher velocities caused by the reduction in channel width from the soot layer do not impact the velocity profile, as the increased velocities in the remaining area still lead to the same average. The pressure is, however, decreased due to the increase in velocity, causing a small decrease in pressure directly at the inlet of the channel. In the inflow channel at the fragmented-layer state, the axial velocity decreases from the prescribed inlet value $\bar{u}_{in}$ to zero, whereas the outflow channel shows the corresponding inverse trend. Compared with the lower-velocity cases of Hafen et al. [16,17], in which the axial velocity decreases more steadily along the channel, at $\bar{u}_{in} = 60\,\text{m s}^{-1}$, the velocity profile shows a different behavior: It decreases only slowly over the length of the channel, but then it decreases rapidly to zero within the last

millimeters. This also leads to a pressure spike at this point of maximum crossover, which can be seen both in the plug state as well as in the converged layer state. For the plug state, this region of maximum crossover and the pressure spike is moved forward by the plug.

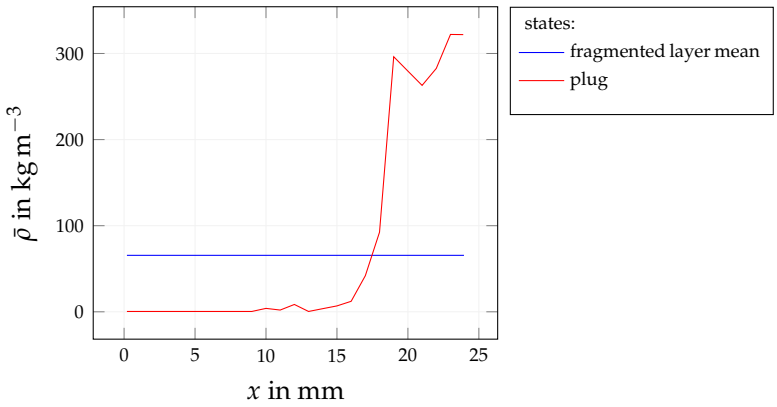

Figure 4. PM density profile $\bar{\rho}(x)$ at fragmented-layer and plug states. Additionally, layout of mean evaluation methodology according to Section 2.

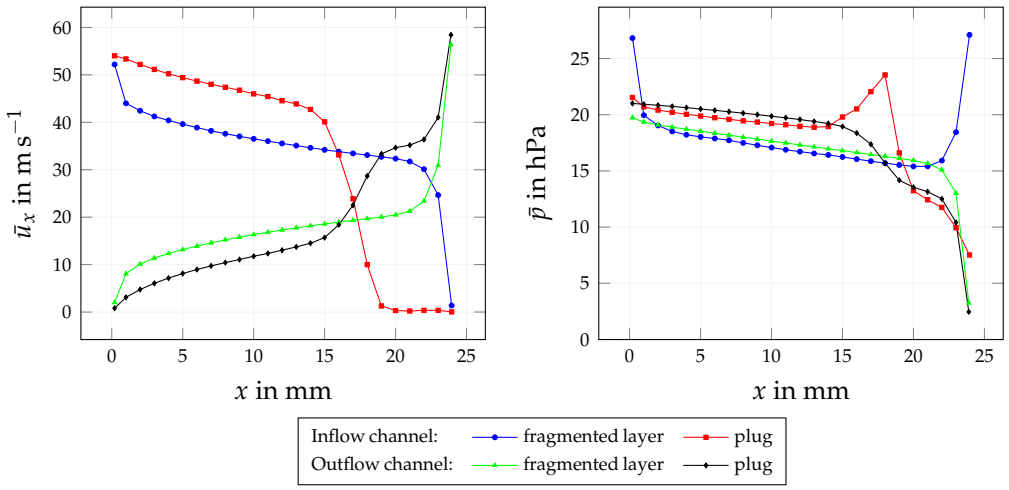

Figure 5. Velocity profile $\bar{u}_x(x)$ and pressure profile $\bar{p}(x)$ in inlet channel domain C_{in} and outlet channel domain C_{out} at fragmented-layer and plug states.

Due to the increased inertia, the majority of air travels to the end of the channel and only then crosses through the porous filter walls.

In the outflow channel, the velocity increases analogously with the decrease in the inflow channel. First, it increases slowly over the channel length and then sharply at the end of the inflow channel, as most gas crosses the porous walls there. In the fragmented-layer state the pressure drops immediately at the channel inlet. The pressure then decreases gradually until it rises sharply again near the back wall. In the outlet channel the pressure decreases continuously as the channel length increases. At the end of the channel, the pressure decreases drastically in the outlet channel at the same time as it increases in the inlet channel, leading to a large pressure difference at the outlet.

Similar behavior can be seen in the plug state. At the beginning of the plug, a local pressure maximum occurs, followed by a rapid decline as the velocity drops to near zero. In the plug state, the inlet channel pressure is 7 hPa lower than in the fragmented-layer state at $x = 0$ mm, as the first fragment row has detached completely. Once a plug is formed, this blocks the flow through the rest of the channel. The pressure spike is therefore moved forward by the plug from the end of the channel. While the plug is not entirely impenetrable, the velocity drastically falls once the flow reaches the left end of the plug.

The increased free substrate area lowers the flow resistance in the remaining open channel section, causing more gas to cross the porous walls in the front and middle regions.

4.2. Reaction

These simulations were carried out to match experiments on the experimental rig described in [9]. In the relevant time frame (the first 4 min), neither in the experiments nor in the simulation did rearrangements occur. The focus of this work was to compare the reaction of the soot particles under realistic conditions of temperature and inlet velocity in the simulation. The model filter channel consists of a rectangular channel with a sintered metal filter element (filtration area: 3 mm × 120 mm). An upstream inlet section of 5 mm extends the channel, promoting a quasi-steady flow field with minimal vortex formation. The channel height is 4 mm. The regeneration was recorded through a quartz-glass window using a high-speed camera (CP90-25P-M72, Optronis GmbH, Kehl, Germany) positioned perpendicular to the channel. The model filter channel was loaded with a reactive soot layer generated by fuel-rich propane combustion using a MiniCAST 6204C soot generator (Jing Ltd., Zollikofen, Switzerland). The operating point of the Jing soot generator was set to 0.05 L min^{-1} propane, 2.0 L min^{-1} quench gas (N_2), and 1.0 L min^{-1} oxidation air. The experimental procedure followed Desens et al. [10,37] and comprised three phases: (i) layer formation at ambient temperature at an inlet gas velocity of 13.2 m s^{-1}, (ii) system heating under inert nitrogen (N_2), and (iii) regeneration with particle-free air. The applied layer containing 18 mg of soot particles had a thickness of approximately 200 µm. An oven was used to heat up the oxidation gas before the channel. The channel was also heated by a heating plate. After deposition and preheating under N_2, the feed was switched to particle-free air to initiate regeneration ($t = 0$ min). During regeneration, the inlet gas velocity was increased to 60 m s^{-1}, and the oxidation-gas temperature was maintained at 823 K. Figure 6 shows the temporal evolution of regeneration along the channel as a time-resolved image sequence. At the beginning the soot layer covers the filter surface. With increasing time, the layer subsequently fragments into discrete soot structures. The magnified region in the center of the channel highlights a progressive increase in fragmentation and a continuous reduction in fragment size between 4 and 16 min.

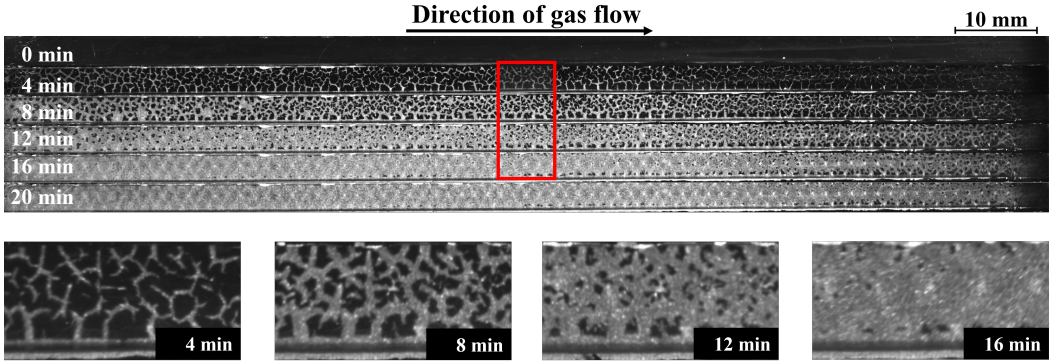

Figure 6. Time-resolved image sequence of the regeneration process of the model filter channel, illustrating the progression from the initiation of regeneration at 0 min to 20 min over the entire channel length. The region marked by the rectangle is shown magnified below, illustrating fragmentation and the decrease in fragment sizes from 4 min to 16 min.

To account for the influence of temperature on the reaction of the particles, a temperature lattice and fragment-local particle temperatures were added to the simulation setup. During each reaction step, for every fragment an average temperature was calculated, which was then used to calculate the local reaction speed. According to the local reaction speed, each fragment was then decreased in size and its particle temperature was increased,

and this temperature increase was then coupled back to the temperature lattice. To be able to compare the resulting pressure loss, the simulation used the two-channel model described in [14]. Because it was not possible to run a simulation of several minutes, only short simulations of 100 ms each were carried out to compare the pressure loss gradient over time at different stages of the regeneration process. For the same reason a reduced channel length was used. Therefore, the total pressure loss is increased compared to experimental results. The number of particles was chosen to be 600 in an evenly spaced grid, similar to the number of fragments at the relevant time in the experiment. In reality, in later stages of the regeneration the number of fragments changes through breakup and oxidation.

Computations were carried out after 0 s, 30 s, and 60 s and after the pressure loss reached a steady state (which corresponds to about 6 min in the experiment). The upper channel of these simulations is depicted in Figure 7. It can be seen that the temperature of the fragments closer to the inlet is about 15 K higher than that at the end of the channel. This is caused by the higher vertical velocity at the end of the channel due to the previously described pressure spike.; cf. Figure 5. This is consistent with the experimental results showing that the oxidation is faster at the inlet of the channel and slower at the end; cf. Figure 6.

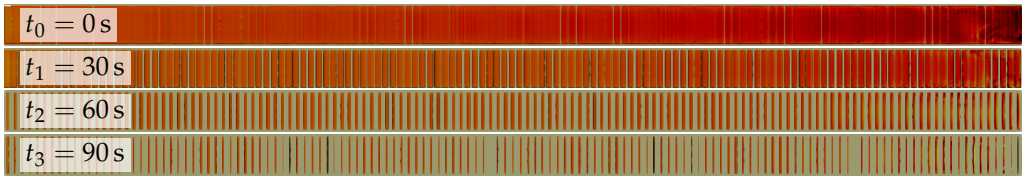

Figure 7. Temperature of particle surface in the numerical simulations, shown in red. From top to bottom: $t_0 = 0\,\mathrm{s}$, $t_1 = 30\,\mathrm{s}$, $t_2 = 60\,\mathrm{s}$, $t_3 = 90\,\mathrm{s}$. The dark yellow background is the porous filter wall below the soot layer.

The normalized pressure loss over time is depicted in Figure 8. The maximum differential pressure at the start of regeneration was normalized to 1, with 0 representing the pressure loss of a fully regenerated, soot-free filter. In the experiment, a drastic decrease in pressure loss during the first minute of the regeneration occurred. After that, the pressure continued to decrease, but much slower. After two minutes, the pressure loss was only 10% above the minimum pressure loss after 10 min. Notably, once the soot layer in the time-resolved image sequence in Figure 6 visibly broke up, the pressure loss was already close to the fully regenerated filter level. The data from the simulations does not fully match the data from the experiments. The rapid decrease in differential pressure at the beginning of the regeneration is correctly predicted, but it occurs slightly earlier than in the experiment. This is likely due to the modeling of the particle fragments. With the beginning of the reaction, they immediately start decreasing in size, leading to reduced pressure losses as soon as the simulation starts. In the experiment, in the first minute only the surface layer reacts and does not immediately create free paths for the fluid. After the first minute the differential pressure decreases more slowly in both experiment and simulation. At the sampled simulation times, the deviation between the normalized experimental and numerical differential pressure values was quantified using the mean absolute error (MAE) and the root-mean-square error (RMSE), resulting in MAE $= 0.131$ and RMSE $= 0.195$ for $z = 9$ data pairs. The larger RMSE shows that the deviation is not uniformly distributed over all sampling points. It is influenced by individual larger deviations, particularly during the earlier decrease in the normalized differential pressure in the simulation.

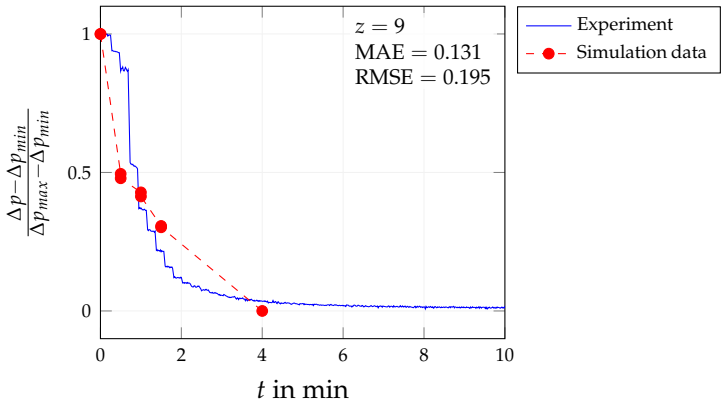

Figure 8. Pressure loss over time during regeneration with particle-free air and a channel inlet velocity of 60 m s^{-1}. Markers indicate the individual simulation data points, while the dashed line is included as a guide to the eye.

5. Conclusions

In this work, previous works about the regeneration processes in wall-flow filters were continued with a focus on realistic operating conditions. Again, these simulations were carried out with the open source software OpenLB 1.8 [39,40]. As a sequel to previous works by Hafen et al. [14–17,19], in this work similar investigations were conducted with a focus on realistic conditions in terms of temperature, inflow speed and the influence of reaction.

In the first part of this work, the influence of realistic inflow speed and temperature on the fragmented-layer state and the plug state was investigated and compared to previous works with lower velocities and ambient air. The total pressure loss increased again, as expected in [17]. Contrary to the findings in [17], the pressure and velocity did not linearly decrease over the channel length under these conditions. Instead, the velocity decreased slowly over the channel length and then rapidly from $u_x = 30\,\mathrm{m\,s^{-1}}$ to zero within the last 3 mm, while the local pressure increased rapidly to the inlet pressure. However, the plug formation and its impact are similar, as in [17]. Again, the plug reduced the effective length of the channel. As it is almost entirely impermeable, the previously described reduction in velocity at the channel end occurred earlier and therefore from a higher velocity, as it did not decrease as much. However, the plug density did not increase compared to previous results, again agreeing with experimental values reported by Kimura et al. [22], Sappok et al. [23] and Dittler [11].

In the second part of this work, the resolved particle model was extended to account for the influence of temperature and reaction of the soot particles. This was achieved by including a temperature lattice and coupling that to the fluid lattice and setting the different heat transfer coefficients. This was then compared with an experiment running a regeneration of a model filter channel. These simulations also showed that the regeneration is slower in the end of the inlet channels because of stronger cooling by advection due to the high velocity through the porous wall and the particle layer at the end of the channel.

A more detailed validation of fragment-size evolution or local oxidation rates is not easily done at this stage, as the simulations start from idealized fragments of uniform size and shape, whereas the experimental layer break-up yields a broad size and shape distribution. Incorporating experimentally derived fragment distributions is therefore a key step for future work, both for the transient rearrangement behavior and for the reaction model.

Author Contributions: Conceptualization, C.G. and M.J.K.; methodology, C.G. and M.J.K.; software, C.G., P.E. and M.J.K.; validation, C.G. and O.D.; formal analysis, C.G., O.D., A.D. and M.J.K.; investigation, C.G.; resources, A.D. and M.J.K.; data curation, C.G.; writing—original draft preparation, C.G., O.D. and A.N.; writing—review and editing, C.G., O.D., A.N., A.D. and M.J.K.; visualization, C.G. and O.D.; supervision, A.D. and M.J.K.; project administration, C.G., A.D. and M.J.K.; funding acquisition, A.D. and M.J.K. All authors have read and agreed to the published version of the manuscript.

Funding: Funded by the Deutsche Forschungsgemeinschaft (DFG, German Research Foundation)—422374351.

Institutional Review Board Statement: Not applicable.

Informed Consent Statement: Not applicable.

Data Availability Statement: No new data were created or analyzed in this study. Data sharing is not applicable to this article.

Acknowledgments: We acknowledge support by the KIT-Publication Fund of the Karlsruhe Institute of Technology. The authors acknowledge support by the state of Baden-Württemberg through bwHPC.

Conflicts of Interest: The authors declare no conflicts of interest.

Abbreviations

The following abbreviations and symbols are used in this manuscript:

Abbreviations	
ADE	advection–diffusion equation
BGK	Bhatnagar–Gross–Krook
LBM	lattice Boltzmann method
MAE	mean absolute error
NSE	Navier–Stokes equation
PM	particulate matter
RMSE	root-mean-square error
TPO	temperature-programmed oxidation
Symbols	
$\boldsymbol{u}$	fluid velocity
p	fluid pressure
$\boldsymbol{x}$	position
t	time
T	temperature
κ	thermal diffusivity
Q	heat source
g_i	discrete distribution function
c_i	discrete lattice speed
w_i	lattice weights
Ω	collision operator
τ_g	fluid relaxation time
c_s	lattice speed of sound
α	mass share
$k_{0,Ox}$	pre-exponential factor of rate coefficient
β	heating rate
E_a	activation energy
n	reaction order
C_S	Smagorinsky constant
$S_{\alpha\beta}$	shear stress tensor
ν_{eff}	effective viscosity

ν_0	laminar viscosity
ν_{turb}	turbulent viscosity
τ^*	effective relaxation time
Pr_t	turbulent Prandtl number
κ_{eff}	effective thermal diffusivity
N	resolution of voxel mesh
$\boldsymbol{u}_p$	particle velocity
$\boldsymbol{\omega}_p$	particle angular velocity
m_p	particle mass
$\boldsymbol{I}_p$	particle's moment of inertia
$\mathrm{Y}_{p,kin}$	particle's kinetic energy
l_x	channel length
l_y	channel width
l_w	wall thickness
$l_{x,s}$	scaled channel length
$\bar{u}_{in}$	average inflow velocity
ρ_p	particle density
ϱ	mean density (along layer and plug)
d_x	fragment's x-dimension
d_{yz}	fragment's equilateral width
F_N	hydrodynamic normal force
$n_{f,x}$	number of fragment rows over channel length
t_{frag}	time at converged fragmented-layer state
t_{plug}	time at final plug state
z	number of data pairs

References

1. Wang, Y.; Kamp, C.J.; Wang, Y.; Toops, T.J.; Su, C.; Wang, R.; Gong, J.; Wong, V.W. The origin, transport, and evolution of ash in engine particulate filters. *Appl. Energy* **2020**, *263*, 114631. [CrossRef]
2. Gaiser, G. Berechnung von Druckverlust, Ruß- und Ascheverteilung in Partikelfiltern. *MTZ—Mot. Z.* **2005**, *66*, 92–102. [CrossRef]
3. Bao, Z.; Chen, H.; Geng, L.; Qi, D.; Wu, H.; Yan, X.; Ji, Z.; Zhang, P.; Sun, F.; Zhang, W. Overview of technological development challenges of diesel particulate filters adapting to future emission regulations. *Chem. Eng. J.* **2025**, *506*, 159982. [CrossRef]
4. Apicella, B.; Mancaruso, E.; Russo, C.; Tregrossi, A.; Oliano, M.M.; Ciajolo, A.; Vaglieco, B.M. Effect of after-treatment systems on particulate matter emissions in diesel engine exhaust. *Exp. Therm. Fluid Sci.* **2020**, *116*, 110107. [CrossRef]
5. Shi, Y.; Cai, Y.; Fan, R.; Cui, Y.; Chen, Y.; Ji, L. Characterization of soot inside a diesel particulate filter during a nonthermal plasma promoted regeneration step. *Appl. Therm. Eng.* **2019**, *150*, 612–619. [CrossRef]
6. Sappok, A.; Govani, I.; Kamp, C.; Wang, Y.; Wong, V. In-Situ Optical Analysis of Ash Formation and Transport in Diesel Particulate Filters During Active and Passive DPF Regeneration Processes. *SAE Int. J. Fuels Lubr.* **2013**, *6*, 336–349. [CrossRef]
7. Ishizawa, T.; Yamane, H.; Satoh, H.; Sekiguchi, K.; Arai, M.; Yoshimoto, N.; Inoue, T. Investigation into Ash Loading and Its Relationship to DPF Regeneration Method. *SAE Int. J. Commer. Veh.* **2009**, *2*, 164–175. [CrossRef]
8. Aravelli, K.; Heibel, A. Improved Lifetime Pressure Drop Management for Robust Cordierite (RC) Filters with Asymmetric Cell Technology (ACT). In *SAE World Congress & Exhibition*; SAE International: Warrendale, PA, USA, 2007. [CrossRef]
9. Thieringer, J.R.D.; Werling, H.; Meyer, J.; Dittler, A. In Situ Tracking of Break-up, Resuspension, and Transport of Reactive Particle Structures in a Single Wall-Flow Filter Channel. *Emiss. Control Sci. Technol.* **2023**, *9*, 149–165. [CrossRef]
10. Desens, O.; Hagen, F.P.; Meyer, J.; Dittler, A. In Situ Observation of Different Soot Layers in a Model Filter Channel During Its Regeneration. In *2025 Stuttgart International Symposium*; SAE Technical Paper; SAE International: Warrendale, PA, USA, 2025. [CrossRef]
11. Dittler, A. Ash Transport in Diesel Particle Filters. In *SAE 2012 International Powertrains, Fuels & Lubricants Meeting*; SAE International: Warrendale, PA, USA, 2012. [CrossRef]
12. Dittler, A. *Abgasnachbehandlung mit Partikelfiltersystemen in Nutzfahrzeugen*, 1st ed.; Wuppertaler Reihe zur Umweltsicherheit: Shaker, Germany, 2014.
13. Wang, Y.; Kamp, C. The Effects of Mid-Channel Ash Plug on DPF Pressure Drop. In *SAE 2016 World Congress and Exhibition*; SAE International: Warrendale, PA, USA, 2016. [CrossRef]

14. Hafen, N.; Dittler, A.; Krause, M.J. Simulation of particulate matter structure detachment from surfaces of wall-flow filters applying lattice Boltzmann methods. *Comput. Fluids* **2022**, *239*, 105381. [CrossRef]
15. Hafen, N.; Thieringer, J.R.; Meyer, J.; Krause, M.J.; Dittler, A. Numerical investigation of detachment and transport of particulate structures in wall-flow filters using lattice Boltzmann methods. *J. Fluid Mech.* **2023**, *956*, A30. [CrossRef]
16. Hafen, N.; Marquardt, J.E.; Dittler, A.; Krause, M.J. Simulation of Particulate Matter Structure Detachment from Surfaces of Wall-Flow Filters for Elevated Velocities Applying Lattice Boltzmann Methods. *Fluids* **2023**, *8*, 99. [CrossRef]
17. Hafen, N.; Marquardt, J.E.; Dittler, A.; Krause, M.J. Simulation of Dynamic Rearrangement Events in Wall-Flow Filters Applying Lattice Boltzmann Methods. *Fluids* **2023**, *8*, 213. [CrossRef]
18. Konstandopoulos, A.G.; Skaperdas, E.; Warren, J.; Allansson, R. Optimized Filter Design and Selection Criteria for Continuously Regenerating Diesel Particulate Traps. In *International Congress & Exposition*; SAE International: Warrendale, PA, USA, 1999. [CrossRef]
19. Hafen, N.; Krause, M.J.; Dittler, A. Simulation of Particle-Agglomerate Transport in a Particle Filter using Lattice Boltzmann Methods. In *22. Internationales Stuttgarter Symposium*; Bargende, M., Reuss, H.C., Wagner, A., Eds.; Springer: Wiesbaden, Germany, 2022; pp. 292–303.
20. Marquardt, J.E.; Römer, U.J.; Nirschl, H.; Krause, M.J. A discrete contact model for complex arbitrary-shaped convex geometries. *Particuology* **2023**, *80*, 180–191. [CrossRef]
21. Marquardt, J.E.; Hafen, N.; Krause, M.J. A novel particle decomposition scheme to improve parallel performance of fully resolved particulate flow simulations. *J. Comput. Sci.* **2024**, *78*, 102263. [CrossRef]
22. Kimura, K.; Lynskey, M.; Corrigan, E.R.; Hickman, D.L.; Wang, J.; Fang, H.L.; Chatterjee, S. Real World Study of Diesel Particulate Filter Ash Accumulation in Heavy-Duty Diesel Trucks. In *Powertrain & Fluid Systems Conference and Exhibition*; SAE International: Warrendale, PA, USA, 2006. [CrossRef]
23. Sappok, A.; Santiago, M.; Vianna, T.; Wong, V.W. Controlled Experiments on the Effects of Lubricant/Additive (Low-Ash, Ashless) Characteristics on DPF Degradation. In Proceedings of the Diesel Engine-Efficiency and Emissions Research (DEER) Conference, Dearborn, MI, USA, 4–7 August 2008.
24. Ferziger, J.H.; Perić, M. *Numerische Strömungsmechanik*; Springer eBook Collection; Springer: Berlin/Heidelberg, Germany, 2008; Volume XV, p. 509S. [CrossRef]
25. Krüger, T.; Kusumaatmaja, H.; Kuzmin, A.; Shardt, O.; Silva, G.; Viggen, E.M. *The Lattice Boltzmann Method - Principles and Practice*; Springer: Cham, Switzerland, 2016. [CrossRef]
26. Hagen, F.; Hardock, F.; Koch, S.; Sebbar, N.; Bockhorn, H.; Loukou, A.; Kubach, H.; Suntz, R.; Trimis, D.; Koch, T. Why Soot is not Alike Soot: A Molecular/Nanostructural Approach to Low Temperature Soot Oxidation. *Flow Turbul. Combust.* **2021**, *106*, 295–329. [CrossRef]
27. Lapuerta, M.; Oliva, F.; Agudelo, J.R.; Boehman, A.L. Effect of fuel on the soot nanostructure and consequences on loading and regeneration of diesel particulate filters. *Combust. Flame* **2012**, *159*, 844–853. [CrossRef]
28. Böhmeke, C.; Wagner, U.; Koch, T. Influence of the air–fuel-ratio and fuel on the reactivity of diesel soot. *Automot. Engine Technol.* **2024**, *9*, 7. [CrossRef]
29. Pope, S.B. *Turbulent Flows*; Cambridge University Press: Cambridge, UK.
30. Nathen, P.; Gaudlitz, D.; Null, M.J.K.; Adams, N.A. On the Stability and Accuracy of the BGK, MRT and RLB Boltzmann Schemes for the Simulation of Turbulent Flows. *Commun. Comput. Phys.* **2018**, *23*, 846–876. [CrossRef]
31. Haussmann, M.; Ries, F.; Jeppener-Haltenhoff, J.B.; Li, Y.; Schmidt, M.; Welch, C.; Illmann, L.; Böhm, B.; Nirschl, H.; Krause, M.J.; et al. Evaluation of a Near-Wall-Modeled Large Eddy Lattice Boltzmann Method for the Analysis of Complex Flows Relevant to IC Engines. *Computation* **2020**, *8*, 43. [CrossRef]
32. Latt, J.; Chopard, B.; Malaspinas, O.; Deville, M.; Michler, A. Straight velocity boundaries in the lattice Boltzmann method. *Phys. Rev. E* **2008**, *77*, 056703. [CrossRef] [PubMed]
33. Skordos, P.A. Initial and boundary conditions for the lattice Boltzmann method. *Phys. Rev. E* **1993**, *48*, 4823–4842. [CrossRef] [PubMed]
34. Ladd, A.J.C. Numerical simulations of particulate suspensions via a discretized Boltzmann equation. Part 1. Theoretical foundation. *J. Fluid Mech.* **1994**, *271*, 285–309. [CrossRef]
35. Thieringer, J.R.D.; Hafen, N.; Meyer, J.; Krause, M.J.; Dittler, A. Investigation of the Rearrangement of Reactive ash; Inert Particulate Structures in a Single Channel of a Wall-Flow Filter. *Separations* **2022**, *9*, 195. [CrossRef]
36. Stephan, P.; Kabelac, S.; Kind, M.; Mewes, D.; Schaber, K.; Wetzel, T. (Eds.) *VDI-WÄrmeatlas*, 12th ed.; Springer: Wiesbaden, Germany, 2019. [CrossRef]
37. Desens, O.; Yavuz, Ö.; Hagen, F.P.; Meyer, J.; Dittler, A. Reactivity influence on carbonaceous particle layer break-up and relocation events in O_2-based model filter regeneration. *Chem. Eng. Sci.* **2026**, *325*, 123467. [CrossRef]

38. Sappok, A.; Rodriguez, R.; Wong, V. Characteristics and Effects of Lubricant Additive Chemistry on Ash Properties Impacting Diesel Particulate Filter Service Life. In *Diesel Exhaust Emission Control 2010*; Technical Report 2010-01-1213; SAE International: Warrendale, PA, USA, 2010. [CrossRef]
39. Krause, M.J.; Kummerländer, A.; Avis, S.J.; Kusumaatmaja, H.; Dapelo, D.; Klemens, F.; Gaedtke, M.; Hafen, N.; Mink, A.; Trunk, R.; et al. OpenLB—Open source lattice Boltzmann code. *Comput. Math. Appl.* **2021**, *81*, 258–288. [CrossRef]
40. Kummerländer, A.; Avis, S.; Kusumaatmaja, H.; Bukreev, F.; Crocoll, M.; Dapelo, D.; Hafen, N.; Ito, S.; Jeßberger, J.; Marquardt, J.E.; et al. *OpenLB Release 1.6: Open Source Lattice Boltzmann Code*; Zenodo: Genève, Switzerland, 2023. [CrossRef]